



## LJMU Research Online

**Tziavos, NI, Gkantou, M, Theofanous, M, Dirar, S and Baniotopoulos, C**

**Behaviour of grout-filled double-skin tubular steel stub-columns: Numerical modelling and design considerations**

<http://researchonline.ljmu.ac.uk/id/eprint/13494/>

### Article

**Citation** (please note it is advisable to refer to the publisher's version if you intend to cite from this work)

**Tziavos, NI, Gkantou, M, Theofanous, M, Dirar, S and Baniotopoulos, C (2020) Behaviour of grout-filled double-skin tubular steel stub-columns: Numerical modelling and design considerations. Structures, 27. pp. 1623-1636. ISSN 2352-0124**

LJMU has developed [LJMU Research Online](#) for users to access the research output of the University more effectively. Copyright © and Moral Rights for the papers on this site are retained by the individual authors and/or other copyright owners. Users may download and/or print one copy of any article(s) in LJMU Research Online to facilitate their private study or for non-commercial research. You may not engage in further distribution of the material or use it for any profit-making activities or any commercial gain.

The version presented here may differ from the published version or from the version of the record. Please see the repository URL above for details on accessing the published version and note that access may require a subscription.

For more information please contact [researchonline@ljmu.ac.uk](mailto:researchonline@ljmu.ac.uk)

<http://researchonline.ljmu.ac.uk/>

1 **TITLE:** Behaviour of grout-filled double-skin tubular steel stub-columns: Numerical  
2 modelling and design considerations

3 **AUTHORS**

4 Nikolaos I. Tziavos<sup>a</sup>, Michaela Gkantou<sup>b</sup>, Marios Theofanous<sup>c</sup>, Samir Dirar<sup>c</sup>, Charalampos  
5 Baniotopoulos<sup>c</sup>

6 **Corresponding author:** Nikolaos I. Tziavos

7 **Email:** [nt431@cam.ac.uk](mailto:nt431@cam.ac.uk)

8 **Affiliations**

9 <sup>a</sup>Centre for Smart Infrastructure and Construction, Department of Engineering, University of  
10 Cambridge, UK

11 <sup>b</sup>Department of Civil Engineering, Liverpool John Moores University, UK

12 <sup>c</sup>Department of Civil Engineering, University of Birmingham, UK

13 

---

14

15 Number of figures: 13

16 Number of tables: 5

17 Nomenclature

18	$A_g$	Cross sectional area of grout core
19	$A_k$	Cross sectional area of hollow part
20	$A_{so}$	Cross sectional area of outer steel tube
21	$A_{si}$	Cross sectional area of inner steel tube
22	$D_o$	External tube diameter
23	$D_i$	Internal tube diameter
24	$D_g$	Grout core diameter
25	$f_{sy_o}$	External steel yield strength
26	$f_{sy_i}$	Internal steel yield strength
27	$f_{sy}$	Steel yield strength
28	$f_{rp}$	Lateral confining pressure
29	$f_{gt}$	Grout tensile strength
30	$f_{gc}$	Compressive strength of grout
31	$f_{cu}$	Compressive strength of cubic sample
32	$f_c$	Compressive cylinder strength
33	$f'_{cc}$	Confined compressive strength
34	$f'_c$	Unconfined compressive strength
35	$L$	Stub-column length
36	$a$	Steel ratio
37	$a_n$	Nominal steel ratio
38	$t_o$	External tube thickness
39	$t_i$	Internal tube thickness
40	$\beta_c$	Post-peak confinement factor
41	$\gamma_c$	Strength reduction factor
42	$\epsilon'_{cc}$	Strain corresponding to confined compressive strength
43	$\bar{\lambda}$	Relative slenderness
44	$\xi$	Confinement factor
45	$\chi$	Hollow ratio, $\chi = \frac{D_i}{D_o - 2t_o}$

46

47 **ABSTRACT**

48 The use of grout-filled double-skin tubular (GFDST) sections in civil, bridge and offshore engineering  
49 applications is rapidly increasing. The design of such composite members is not directly covered by  
50 design codes, despite recent research studies investigating their performance, proposing design  
51 equations or modifying existing codified methods. Aiming to extend the available pool of structural  
52 performance data, the current study reports the results of an extensive numerical investigation on  
53 GFDST stub-columns. Finite element (FE) models, are developed and validated against published test  
54 data. A parametric investigation is conducted to evaluate the effect of key parameters, including cross-  
55 sectional slenderness, hollow ratio and the effect of concrete infill on the capacity of GFDST members.  
56 The numerically obtained load capacities along with collated test data are utilised to assess the  
57 applicability of design strength predictions based on European Code (EC4), the American Concrete  
58 Institute (ACI) and the analytical models proposed by Han et al. and Yu et al. Overall, the modified Yu  
59 et al. provided strength predictions with low scatter, whereas ACI yielded overly conservative  
60 predictions particularly for smaller hollow ratios.

61 **Keywords:** Composite columns, Double skin, Grout-filled, Finite element modelling

62 **Highlights**

- 63 ■ Numerical investigations on the performance of circular grout-filled double skin stub-columns.  
64 ■ A parametric study was carried out to evaluate the influence of hollow ratio for varying cross  
65 sections on the compressive resistance.  
66 ■ Assessment of codified methods and analytical models was performed.

67

## 68 1. Introduction

69 Concrete-filled tubular members are extensively employed in the construction of bridges, high-  
70 rise buildings, transmission towers and offshore structures [1, 2]. The surrounding tube provides  
71 confinement to the concrete core thus increasing its strength and ductility, whilst the concrete infill  
72 prolongs the occurrence of local buckling of the steel tube [3, 4]. Hence, they possess superior stiffness,  
73 strength and ductility compared to their bare steel or reinforced concrete counterparts resulting in  
74 smaller section sizes and larger lettable areas in the lower stories of multi-storey buildings [5]. In recent  
75 years, concrete-filled double skin tubular (CFDST) sections – where concrete is used to fill the annulus  
76 of two steel hollow sections, are attracting more interest, offering a lighter-weight alternative with  
77 enhanced stiffness, greater bending capacity, along with improved fire and seismic resistance [6-10].

78 In offshore construction, the infill material is typically a cement-based grout, resulting in grout-  
79 filled double skin tubular (GFDST) members. Such members are typically employed in oil and gas  
80 jacket platforms and offshore wind turbine foundations to form grouted connections [11] or as a  
81 remediation solution for lifetime extension as offshore structures in the North Sea are close to end-of-  
82 life [12]. Tubular double-skin filled members combining carbon and stainless steel [13, 14] are also  
83 used in submarine pipelines [13]. For offshore applications, GFDSTs with circular hollow sections  
84 (CHSs) are the configuration attracting more interest, as they provide the highest level of confinement  
85 on the sandwiched grout core [9, 15].

86 To better understand the response of this type of composite members, several researchers have  
87 experimentally investigated the strength of CFDST stub-columns and beam-columns with CHS tubes  
88 [6, 16-21]. The performance of different cross section shapes has also been evaluated in experimental  
89 studies, including CFDST with square hollow sections [22], rectangular hollow sections [23] and a  
90 combination of CHS and square hollow sections [16]. Han et al. [24] tested CFDST beam-columns with  
91 CHS and square cross-section under cyclic loads, whereas impact [25] and torsional tests [26] are also  
92 reported in the literature. Alternatives to carbon steel have been considered for structural applications  
93 in corrosive environments such as stainless steel [27-29] and aluminium [30], while the use of  
94 alternative cementitious composites such as rubberised concrete [31] has been urged by the need to  
95 minimise carbon emissions. Along with the aforementioned studies and to enhance the design practice  
96 of double-skinned composite members, researchers have conducted numerical investigations on the  
97 influence of material and geometrical parameters to generate new data and assess existing design  
98 methods [10, 13, 32-35].

99 Tests on GFDST members are scarce; Li et al. [12] reported 8 tests on stub-columns, 4 beam-  
100 columns and 2 on GFDST beams. Although the behaviour of the grout is often treated in a similar  
101 manner to that of concrete, for GFDSTs the grouted annulus is often very small resulting in higher  
102 hollow ratio ( $\chi$ ) values. Hollow ratio is the ratio of the internal steel diameter to the internal diameter  
103 of the external steel tube and is a commonly used metric in CFDSTs to provide information on the

104 cross-sectional geometry. Typical hollow ratios in previous experimental studies range from 0.2 to 0.7,  
105 whereas in offshore construction of GFDST, members with hollow ratios greater than 0.8 are often  
106 employed. The ultimate strength of GFDST stub columns, is a function of the steel yield strength ( $f_{sy}$ ),  
107 the grout material compressive strength ( $f_{gc}$ ) and the steel cross sectional properties (diameter to  
108 thickness ratio,  $D/t$ ).

109 The present paper aims to fill this gap of limited available data on the structural performance of  
110 GFDST cross-sections across a range of hollow ratios by generating new data on the compressive  
111 capacity of GFDST stub columns by means of numerical modelling. Initially, the developed FE models  
112 are validated against experiments and subsequently a parametric study is carried out, investigating the  
113 effect of cross-sectional slenderness in small and large-diameter GFDST stub-columns. The hollow  
114 ratios for the developed FE models range from 0.4 to 0.9. The numerically obtained strengths are  
115 subsequently compared with design strength predictions obtained from European Code EN 1994-1-1  
116 (EC4) [36], American Concrete Institute (ACI) [37] and the analytical models proposed by Han et al.  
117 [8] and Yu et al. [38].

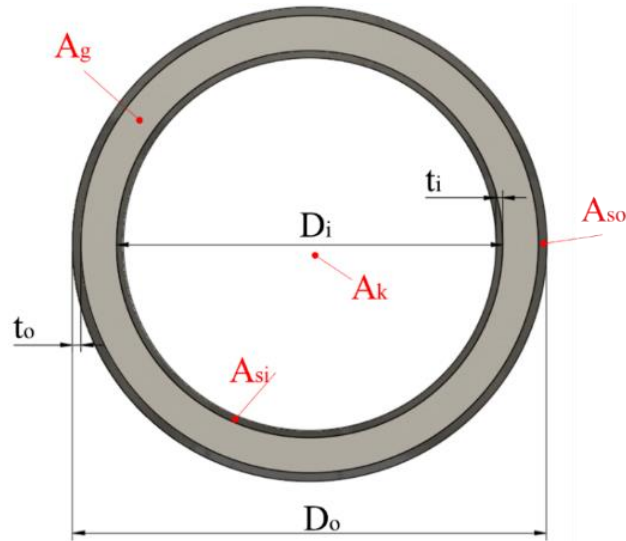
## 118 **2. Numerical modelling**

119 The general-purpose FE software Abaqus [39] was employed for the numerical computations. In  
120 order to verify the accuracy of the numerical simulations, the numerical model was validated against  
121 test data reported in two experimental studies [6, 12], which are briefly discussed in Section 2.1.  
122 Sections 2.2 and 2.3 provide a detailed description on the numerical modelling assumptions, including  
123 the type of analyses, the adopted boundary conditions, interaction properties and the employed material  
124 models for the steel and the infill.

### 125 **2.1 Selected experimental tests**

126 The experiments on stub columns reported by Tao et al. [6] and Li et al. [12] are used herein to  
127 validate the FE models. The infill material in the tests reported in [6] is concrete with a compressive  
128 strength of 47.4 N/mm<sup>2</sup>, whereas a grout infill with a compressive strength of 51.1 and 54.8 N/mm<sup>2</sup> was  
129 used in the tests reported in [12]. A total of 7 cross-section geometries were considered, with duplicate  
130 tests performed for each configuration thereby resulting in 14 experimental tests. The hollow ratio of  
131 the selected experimental tests ranges from 0.28 to 0.84. The dimensions of each specimen and the  
132 corresponding material properties are reported in Table 1, where  $L$  is the length of the specimen and  
133  $D_o$ ,  $t_o$ ,  $D_i$ ,  $t_i$ , the diameter and thickness of the external and internal steel tube respectively. A typical  
134 GFDST cross-section is shown in Figure 1, where  $A_{so}$  and  $A_{si}$  are the cross-sectional areas of the outer  
135 and the inner tube respectively,  $A_g$  the cross-sectional area of the grout and  $A_k$  the area of the hollow  
136 part. The average yield strength of the external ( $f_{syo}$ ) and internal steel tubes ( $f_{syi}$ ), as obtained from

137 tensile coupon tests, along with the cubic compressive strength ( $f_{cu}$ ) and the recorded ultimate  
 138 compressive strength ( $P_{u,test}$ ) are also reported in Table 1.



139

140 Figure 1: Geometric properties and notation for GFDST members

141 Table 1: Dimensions and material properties of circular double skin stub-column specimens used in the  
 142 validation study

Source	Test ID	Dimensions (mm)					Material properties			
		$D_o$	$t_o$	$D_i$	$t_i$	$L$	$f_{syo}$ (N/mm <sup>2</sup> )	$f_{syi}$ (N/mm <sup>2</sup> )	$f_{cu}$ (N/mm <sup>2</sup> )	$P_{u, test}$ (kN)
[6]	cc2a	180	3	48	3	540	275.9	396.1	47.4	1790
	cc2b	180	3	48	3	540	275.9	396.1	47.4	1791
	cc3a	180	3	88	3	540	275.9	370.2	47.4	1648
	cc3b	180	3	88	3	540	275.9	370.2	47.4	1650
	cc4a	180	3	140	3	540	275.9	342	47.4	1435
	cc4b	180	3	140	3	540	275.9	342	47.4	1358
	cc5a	114	3	58	3	342	294.5	374.5	47.4	904
	cc5b	114	3	58	3	342	294.5	374.5	47.4	898
[12]	GC1-1	140	2.5	114	2	420	307	321	51.1	751.80
	GC1-2	140	2.5	114	2	420	307	321	51.1	698.86
	GC2-1	140	2.5	76	1.6	420	307	321	51.1	935.81
	GC2-2	140	2.5	76	1.6	420	307	321	51.1	928.62
	GCL-1	450	8	400	8	700	365	363	54.8	8867.92
	GCL-2	450	8	400	8	700	365	363	54.8	8735.85

## 143 2.2 Modelling assumptions

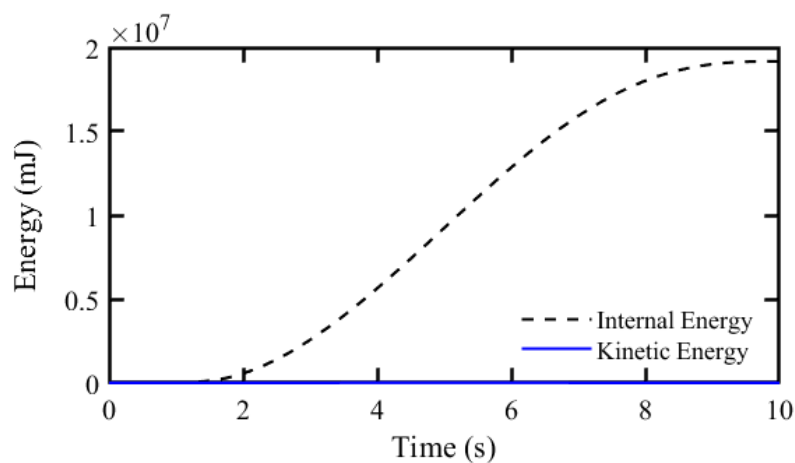
144 The loading and support conditions used in the experimental set-up were reflected in the  
 145 boundary conditions and constraints adopted in the FE models. The boundary conditions were applied  
 146 to two reference points, one on each end of the member, to which the degrees of freedom of the nodes  
 147 of top and bottom cross-section of the model were tied. For each of the modelled tests the employed  
 148 boundary conditions and constraints are shown in Figure 3a. Translation along the z-axis (i.e. parallel  
 149 to the member axis) was allowed at the top reference points, with all remaining degrees of freedom  
 150 restrained at both reference points. The FE models were based on the reported dimensions [6, 12] and

151 the steel and grout parts were discretised using linear solid elements with reduced integration (C3D8R).  
152 A mesh convergence study has been initially performed and a minimum of three elements have been  
153 used along the thickness of the steel plates and grout [40], respectively, as shown in Figure 3b, to  
154 produce accurate and computationally efficient results.

155 A quasi-static explicit solution scheme was selected in order to avoid convergence difficulties  
156 arising during the conventional implicit analysis due to the non-monotonic nature of the concrete  
157 response [41]. This approach alleviates convergence issues, however it is sensitive to the selected  
158 loading rate requiring engineering judgment on the computational results.

159 In this case, the step time was set at 10 s and a sufficiently small time increment was selected  
160 ( $10^{-4}$ ) through a sensitivity analysis, ensuring that the inertia effects and artificial strain energy were  
161 negligible during the simulations. This was subsequently verified by ensuring that the kinetic energy  
162 remained smaller than 2% of the internal strain energy throughout the analysis. As an example this is  
163 illustrated in Figure 2. The load was applied using displacement control with a smooth amplitude  
164 function. Contact at the steel-grout interfaces was modelled using the general contact algorithm. In the  
165 normal direction, a hard contact formulation was chosen and a friction coefficient ( $\mu$ ) of 0.4 was  
166 assigned for the tangential direction [41].

167 Geometric imperfections and residual stresses are known to affect the response of axially loaded  
168 compressive tubular members. However, in GFDST members their influence is considerably reduced  
169 due to the presence of the infill material providing lateral restraint, which lessens the sensitivity of the  
170 tubes to local buckling and can therefore be ignored in the numerical analysis. This is in line with past  
171 studies [27] and as shown in Section 3, this assumption did not have any implication on the accuracy  
172 of the FE models.

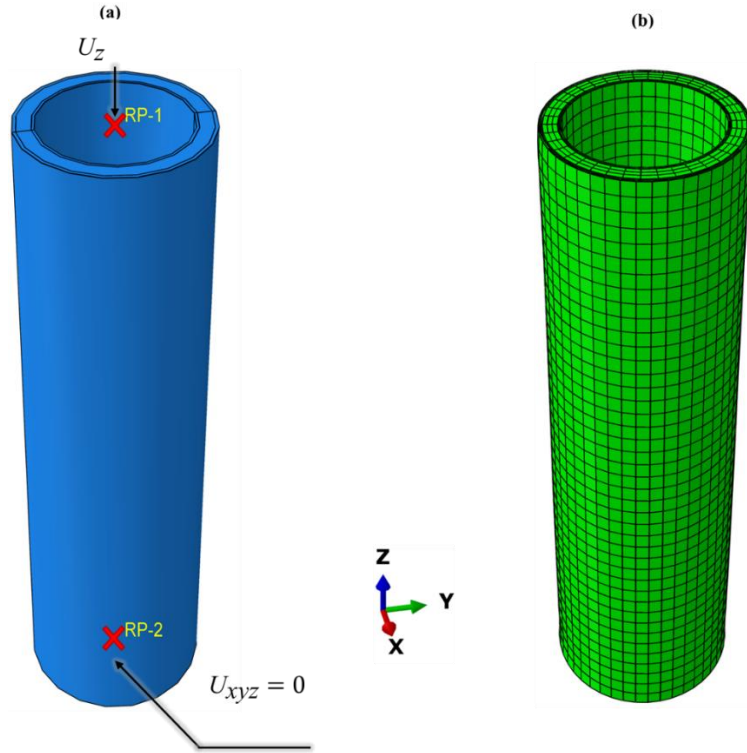


173

174

Figure 2: Comparison between internal and kinetic energy for specimen cc4a, b





175

176

Figure 3: a) Boundary conditions on stub column finite element model and b) Typical mesh discretisation

177

### 2.3 Material modelling

178

179

180

181

182

183

184

For the steel tubulars the von Mises yield criterion with an isotropic hardening behaviour was used. The behaviour of the steel tubes was defined with a multi-linear stress-strain curve employing the yield and ultimate stress values and corresponding strains, which were experimentally obtained and reported in [12]. Cold-formed steel tubes were used in the experiments conducted by Tao et al. [6]. The yield strength for each steel section is given in Table 1, whereas the Poisson's ratio ( $\nu$ ) was set at 0.3. The engineering stress ( $\sigma_{eng}$ ) and strain ( $\epsilon_{eng}$ ) values were converted to true stress ( $\sigma_{true}$ ) and strain ( $\epsilon_{true}$ ) following equations (1) and (2):

$$\sigma_{true} = \sigma_{eng}(1 + \epsilon_{eng}) \quad (1)$$

$$\epsilon_{true} = \ln(1 + \epsilon_{eng}) - \left(\frac{\sigma_{true}}{E}\right) \quad (2)$$

185

186

187

188

189

190

191

192

Typical cement-based grouts exhibit similar behaviour to concrete in compression, although a larger scatter is to be expected in test results. For this purpose, for the subsequent analyses an analytical concrete model has been employed to describe the behaviour of the infill material in compression. In addition, to account for the restraint on the core from the steel tubes, a confined concrete model described in Ref. [15] was selected. An exemplary stress-strain curve when using the aforementioned analytical model is depicted in Figure 4 comprising three stages and is described herein. The first part of the confined stress-strain curve (AB) is described by equation (1), which was suggested by Mander et al. [42].

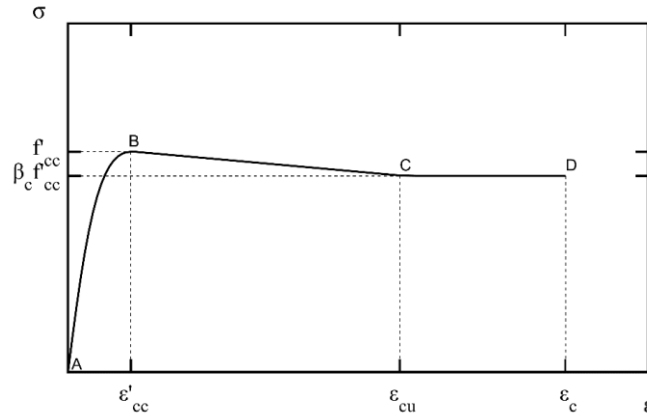
$$\sigma_c = \frac{f'_{cc} \lambda (\varepsilon_{cc} / \varepsilon'_{cc})}{\lambda - 1 + (\varepsilon_c / \varepsilon'_{cc})^\lambda}, \quad \varepsilon_c < \varepsilon'_{cc} \quad (3)$$

$$\text{where } \lambda = \frac{E_c}{E_c - (f'_{cc} / \varepsilon'_{cc})} \quad (4)$$

193 and  $f'_{cc}$ ,  $\varepsilon'_{cc}$  are the confined compressive strength and corresponding strain,  $\varepsilon_c$  the compressive strain  
 194 and  $E_c$  the Young's modulus. In this study the experimentally defined Young's modulus, reported in  
 195 [12] is used in the numerical models.

$$f'_{cc} = \gamma_c f'_c + k_1 f_{rp} \quad (5)$$

$$\varepsilon'_{cc} = \varepsilon'_c \left( 1 + k_2 \frac{f_{rp}}{\gamma_c f'_c} \right) \quad (6)$$



196

197

Figure 4: Exemplary stress-strain curve for confined concrete

198

199

200

201

For the constants  $k_1$  and  $k_2$ , values of 4.1 and 20.5 as suggested in Richart et al. [43] were used, whereas  $\varepsilon'_c$  is the unconfined concrete strain at  $f'_c$  and  $\gamma_c$  a strength reduction factor to account for material imperfections and  $D_g$  is the diameter of the grout core. The lateral confining pressure ( $f_{rp}$ ), on the grout is obtained from equation (9) as it satisfies the cross-sections under investigation.

$$\varepsilon'_c = 0.002 + \left( \frac{\gamma_c f'_c - 28}{5400} \right), \quad 28 \leq \gamma_c f'_c \leq 82 \quad (7)$$

$$\gamma_c = 1.85 D_g^{-0.135}, \quad 0.85 \leq \gamma_c \leq 1.0 \quad (8)$$

$$f_{rp} = \left( 0.006241 - 0.0000357 \frac{D}{t} \right) f_{syo}, \quad 47 \leq D/t \leq 150 \quad (9)$$

202

203

The second (BC) and third (CD) stages of the stress-strain curve are described by equations (10) and (11) respectively.

$$\sigma_c = \beta_c f'_{cc} + \left( \frac{\epsilon_{cu} - \epsilon_c}{\epsilon_{cu} - \epsilon_{cc}} \right) (f'_{cc} - \beta_c f'_{cc}), \epsilon_{cc} \leq \epsilon_c \leq \epsilon_{cu} \quad (10)$$

$$\sigma_c = \beta_c f'_{cc}, \epsilon_c > \epsilon_{cu} \quad (11)$$

204 where  $\beta_c$  accounts for any confinement after the peak load was reached and was expressed in [44] as  
 205 follows:

$$\beta_c = 0.0000339 + \left( \frac{D}{t} \right)^2 - 0.10085 \left( \frac{D}{t} \right) + 1.3491 \quad (12)$$

206 Subsequently, the analytical compressive stress-strain curve was converted to true values and  
 207 employed in the finite element model with the Concrete Damaged Plasticity model. In this study,  
 208 following a sensitivity analysis, a dilation angle equal to  $20^\circ$  was found to result in good agreement with  
 209 the experimental tests. For the remaining parameters, the eccentricity was set equal to 0.1, the ratio of  
 210 equibiaxial to uniaxial compressive stress  $f_{b0}/f_{c0}$  was taken equal to 1.16 and finally the ratio of the  
 211 second stress invariant on the tensile meridian to that on the compressive meridian at initial yield was  
 212 set equal to 0.725 as per [45]. The tensile strength of the grout was estimated from equation (13) as  
 213 suggested in [46] and a stress-displacement curve was defined for the tensile response of the infill  
 214 material.

$$f_{gt} = 0.3(f_{ck})^{2/3} \quad (13)$$

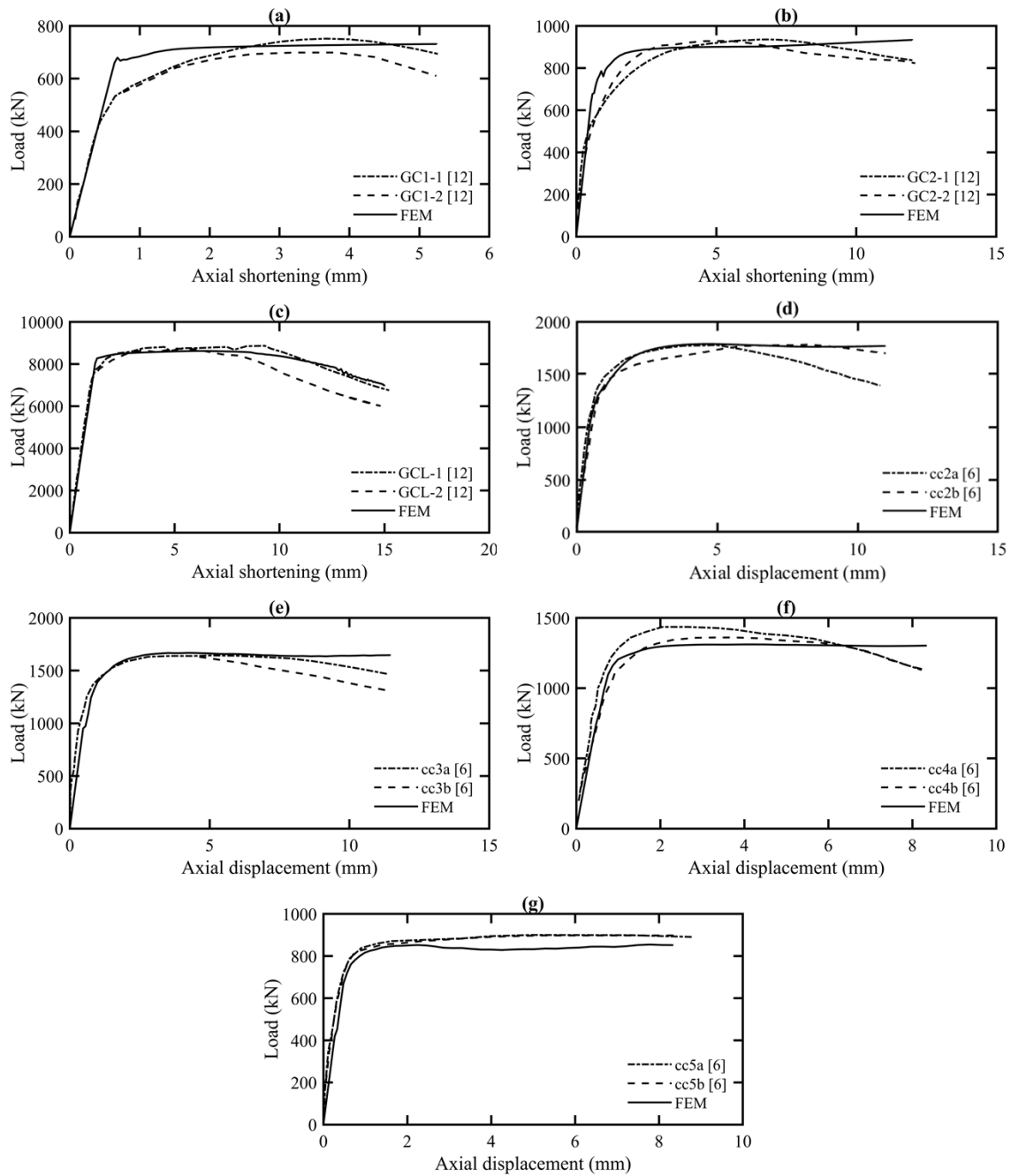
### 215 3. Validation

216 The FE models were verified against the experimental tests reported in Refs. [6, 12]. The comparison  
 217 between the tests and the numerical models was based on the load-displacement response, the observed  
 218 failure modes and the ultimate axial capacity. In Figure 5 the experimental and the numerical load –  
 219 axial displacement response is compared. The initial stiffness has been accurately simulated in all the  
 220 examined cases, demonstrating that the elastic constants and boundary conditions were accurately  
 221 modelled. In all the models the ultimate load is also well captured. The ultimate load ( $P_{u, test}$ ), is  
 222 compared with the numerically-obtained one ( $P_{u, FE}$ ) in Table 2, showing very good agreement, with an  
 223 average ratio of 1.018 and a COV of 0.033. Typical buckling modes in filled double-skin members  
 224 include outward buckling of the external tube, inward/outward buckling of the internal tube and  
 225 crushing/cracking of the infill medium. This is confirmed in Figure 6, where a comparison of the  
 226 experimental and numerical failure modes is made. The observed outward buckling of the external and  
 227 internal steel tubes and grout/concrete crushing is accurately captured for different models. As shown  
 228 in Figure 5, the post-peak behaviour which was recorded in some of the experiments has not been very  
 229 well captured by the numerical model, which is possibly attributed to the employed analytical concrete  
 230 model and the plateau it forms until it reaches the ultimate strain, as illustrated in Figure 4 and was also

231 suggested by Thai et al. [47]. It is considered that this did not have any impact on the primary focus of  
 232 this paper, i.e. the ultimate load that has been captured with great precision. Overall, it is demonstrated  
 233 that from the validation study the numerical models provide an accurate representation of the real  
 234 conditions and a precise prediction of the experimentally observed ultimate load and corresponding  
 235 failure modes which are subsequently used for the analytical assessment.

236 Table 2: Comparison of ultimate strength of FE models against test results

Source	Test ID	$P_{u, test}$ (kN)	$P_{u, FE}$ (kN)	$P_{u, test/FE}$
Tao et al. [6]	cc2a	1790	1780.19	1.005
	cc2b	1791	1780.19	1.006
	cc3a	1648	1668.61	0.987
	cc3b	1650	1668.61	0.988
	cc4a	1435	1311.05	1.094
	cc4b	1358	1311.05	1.035
	cc5a	904	854.54	1.057
	cc5b	898	854.54	1.050
Li et al. [12]	GC1-1	751.80	731.10	1.028
	GC1-2	698.86	731.10	0.956
	GC2-1	935.81	933.60	1.002
	GC2-2	928.62	933.60	0.995
	GCL-1	8867.92	8622.52	1.028
	GCL-2	8735.85	8622.52	1.013
<b>Average</b>				<b>1.017</b>
<b>COV</b>				<b>0.033</b>

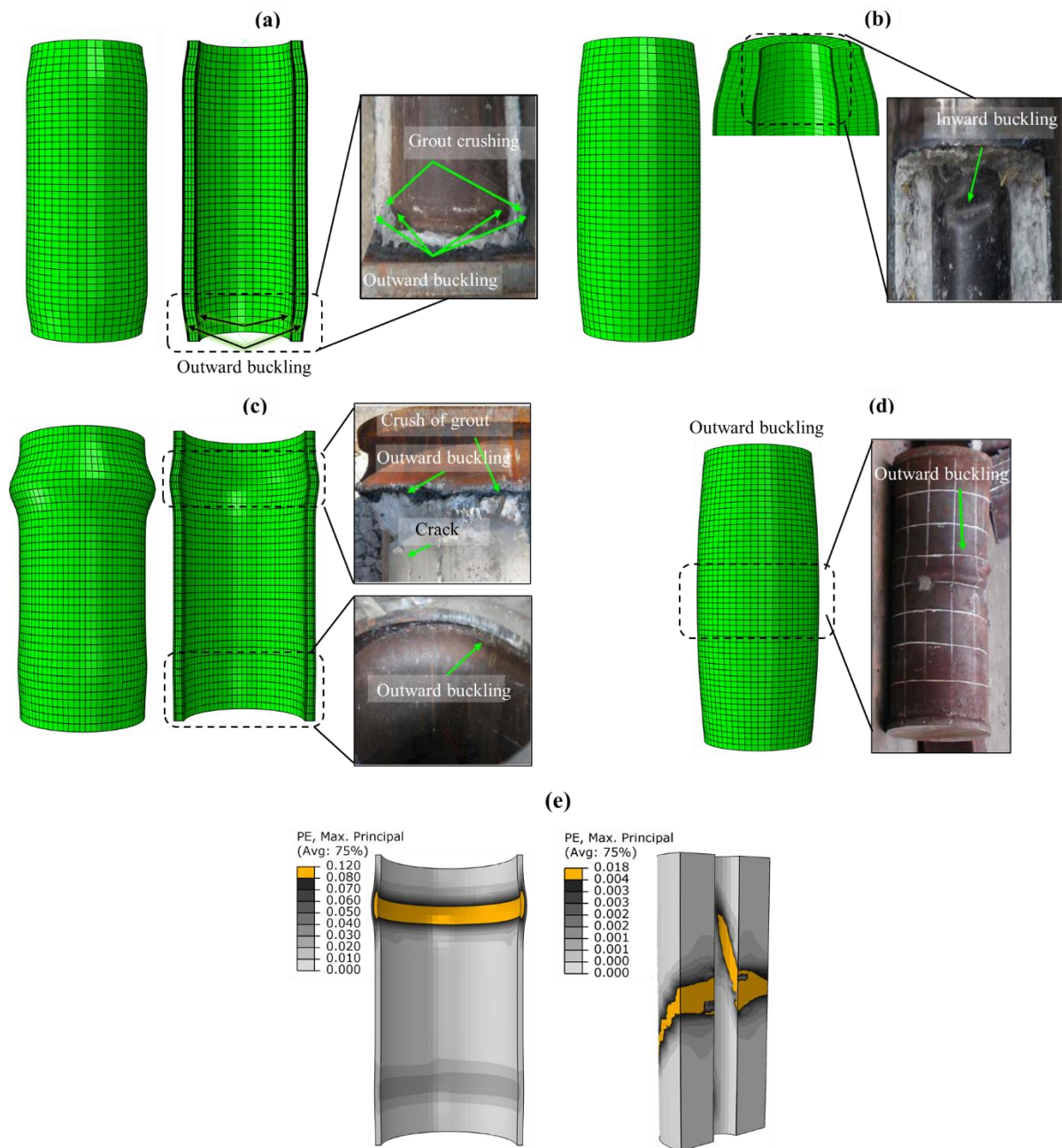


238

239

240

Figure 5: Comparison of axial load-shortening curves for experimental and FE models for stub-columns



241

242 Figure 6: Failure mode comparison between experiments and FE models for tests a) GC1-2, b) GC2-1, c) GCL-  
 243 1, d) cc3a and infill material crushing for GCL-1 and cc3a

244 **4. Parametric study**

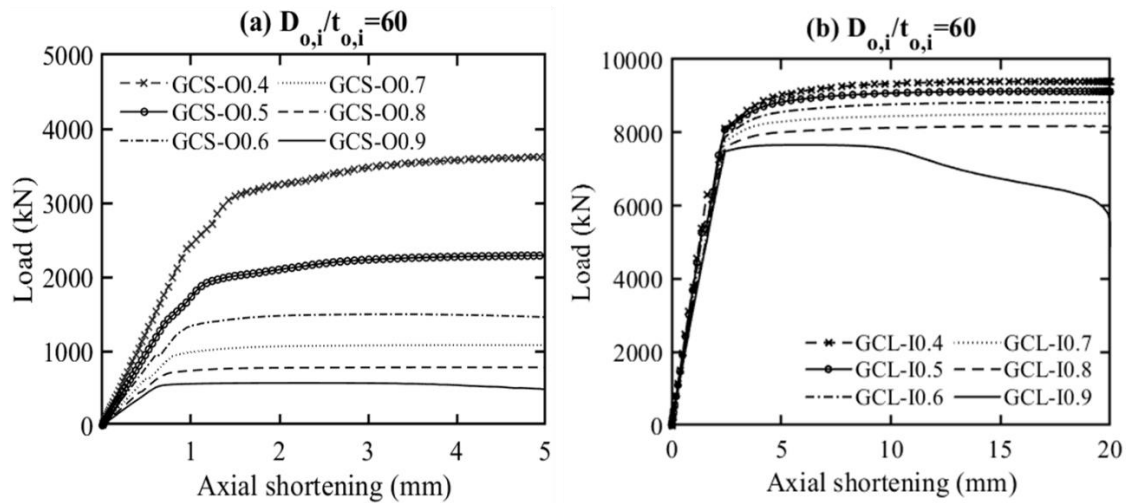
245 Upon successful validation, the numerical models were utilised to conduct an extensive  
 246 parametric analysis, aiming to investigate the effect of key parameters on the structural response of  
 247 GFDST stub-columns. The validated models included two cross-sections with external diameters equal  
 248 to 140 mm and 450 mm. Using these models as a basis, two groups were considered; one with a small  
 249 (group GCS) and one with a large diameter (group GCL). In order to get an accurate representation of  
 250 the cross-sectional response, for the numerical models the length of the stub-columns was taken equal  
 251 to 3 times the external diameter. The effect of the diameter-to-thickness ratio was examined and four

252 cross-sectional slenderness values equal to 50, 60, 70 and 80 (abbreviated as Dt50, Dt60, Dt70 and  
253 Dt80) were investigated for each of the GCS and GCL groups. For the parametric study, the external  
254 and internal steel tubes were set to have equal D/t ratios on all FE models and the hollow ratio effect is  
255 further investigated in the remaining sections.

#### 256 4.1 Cross-sectional slenderness

257 For each one of the D/t values, six hollow ratio values ranging from 0.4 to 0.9 with a step of 0.1  
258 were considered. By maintaining a constant diameter to thickness ratio for both the external and the  
259 internal steel tube, the same hollow ratio value  $\chi$  can be achieved by either varying the diameter and the  
260 thickness of the outer tube and keeping the inner tube dimensions constant or vice versa. Both cases  
261 have been investigated and are designated as I (followed by the  $\chi$  value) or O (followed by the  $\chi$  value),  
262 depending on whether the inner or outer tube dimensions have been modified. Adopting the same  
263 assumptions described in Section 2, a total of 96 nonlinear analyses were carried out and the results are  
264 reported in this section.

265 The full load-displacement path was captured during the analysis and typical cases for a small  
266 scale and a large scale stub column with D/t=60 are shown in Figure 7a and Figure 7b respectively.  
267 Note that for the cases with flat load-displacement post-elastic response, where a clear peak value was  
268 not observed, the maximum load that was recorded during the simulation was considered to be the  
269 ultimate load. In both cases, the effect of the change in the hollow ratio value is evident. In Figure 7a  
270 the inner steel tube has been kept constant, while in Figure 7b, the outer steel tube geometric properties  
271 are constant for the examined hollow ratios. As anticipated, a smaller hollow ratio that corresponds to  
272 a larger grout thickness increases the axial capacity the GFDST stub-column. This is more pronounced  
273 in Figure 7a where the outer tube has been modified indicating that the influence of the external steel  
274 tube is higher. In most cases, the overall response does not present a sudden loss of strength but rather  
275 a stable ductile post-peak response, which is similar to the behaviour reported in the experiments (see  
276 Figure 5).

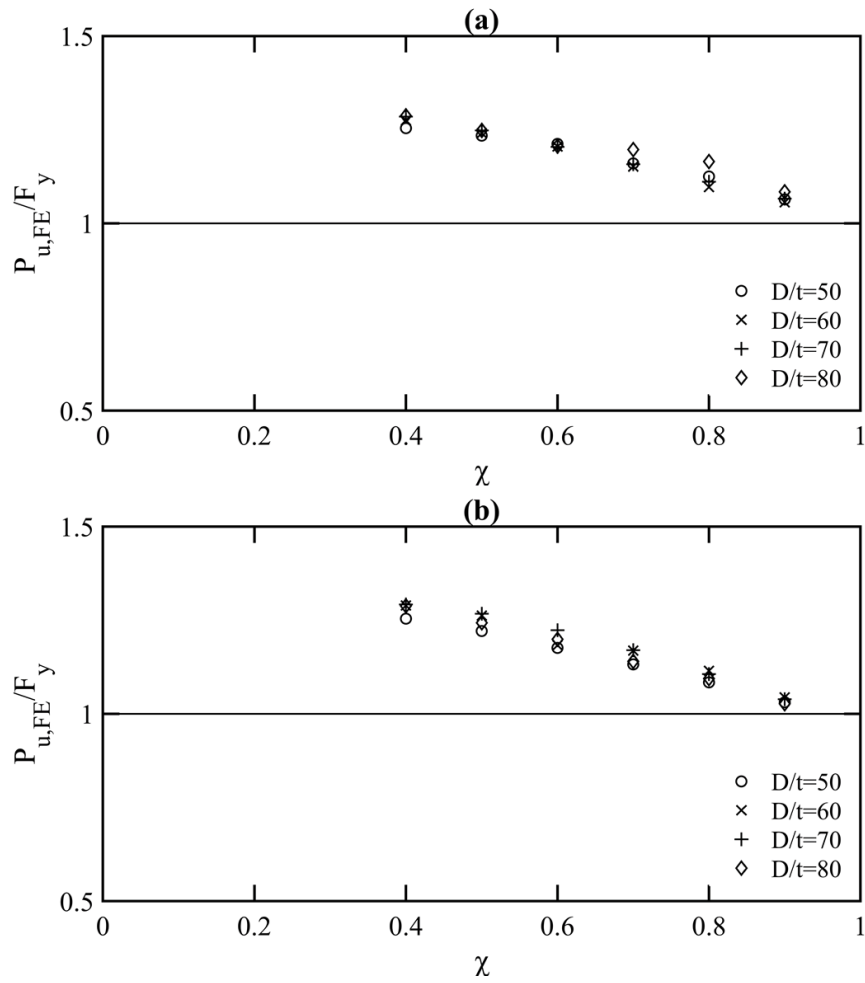


277

278 Figure 7: Typical load-displacement curves from parametric models for a) varying external tube and b) varying  
 279 internal tube

280 In Figure 8 and Figure 9 the numerically obtained failure loads are normalised against the  
 281 squash load ( $F_y$ ), and are plotted against the hollow ratio for the small (GCS group) and large diameter  
 282 (GCL group) FE models respectively. The squash load is defined as the sum of three terms, which are  
 283 the products of the yield strength and the cross section of the two steel tubes and the product of the  
 284 compressive strength of the grout with the cross section of the grout. For each group two cases were  
 285 investigated, one with a constant outer steel tube and one with a constant inner steel tube. As previously  
 286 observed in Figure 7, an increase in the value of hollow ratio, decreases the normalised compressive  
 287 strength of the stub column for all the considered models of the GCS group (Figure 8a, b). The same  
 288 conclusions are also drawn from the FE models in the GCL group specimens for constant outer and  
 289 inner tubes, as shown in Figure 9a and Figure 9b respectively. In particular, for GCS with constant  
 290 external tube, the normalised load was in the range of 1.28 to 1.05 for hollow ratio equal to 0.4 and 0.9,  
 291 respectively. The same ratios were equal to 1.29 to 1.02 for GCS with constant inner tube, 1.36 to 1.03  
 292 for GCL with constant external tube and 1.29 to 1.04 for GCL with constant inner tube. In addition, no  
 293 clear effect of the  $D/t$  value on the normalised load was observed.

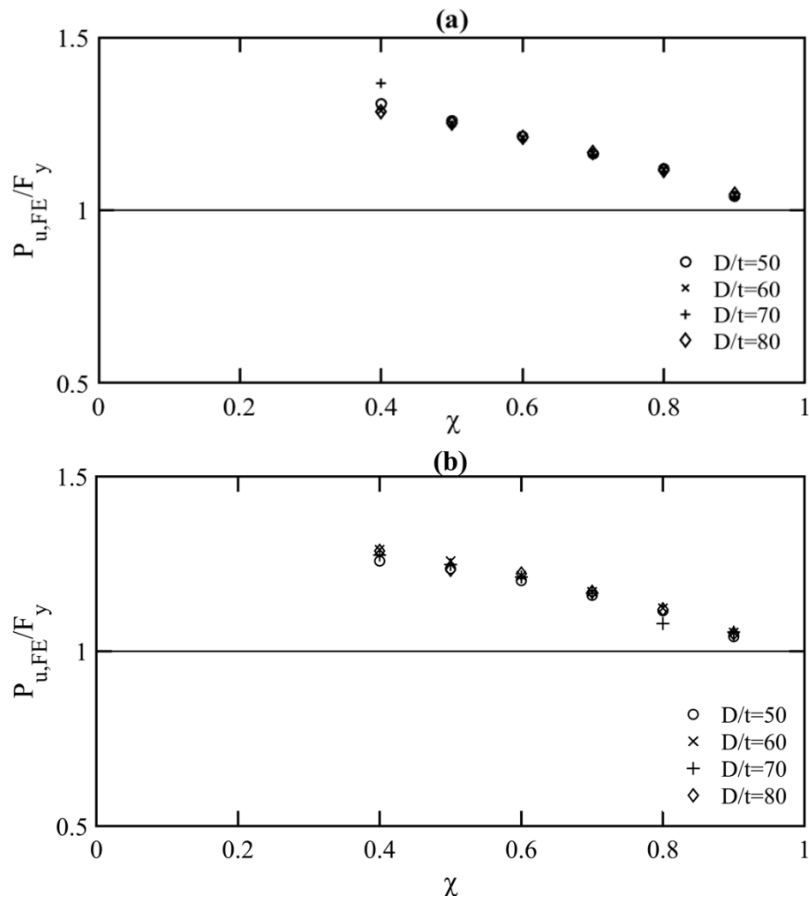




294

295  
296

Figure 8: Effect of steel tube cross section on the axial compressive strength of FE models in group GCS for a) constant external tube and b) constant inner tube



297

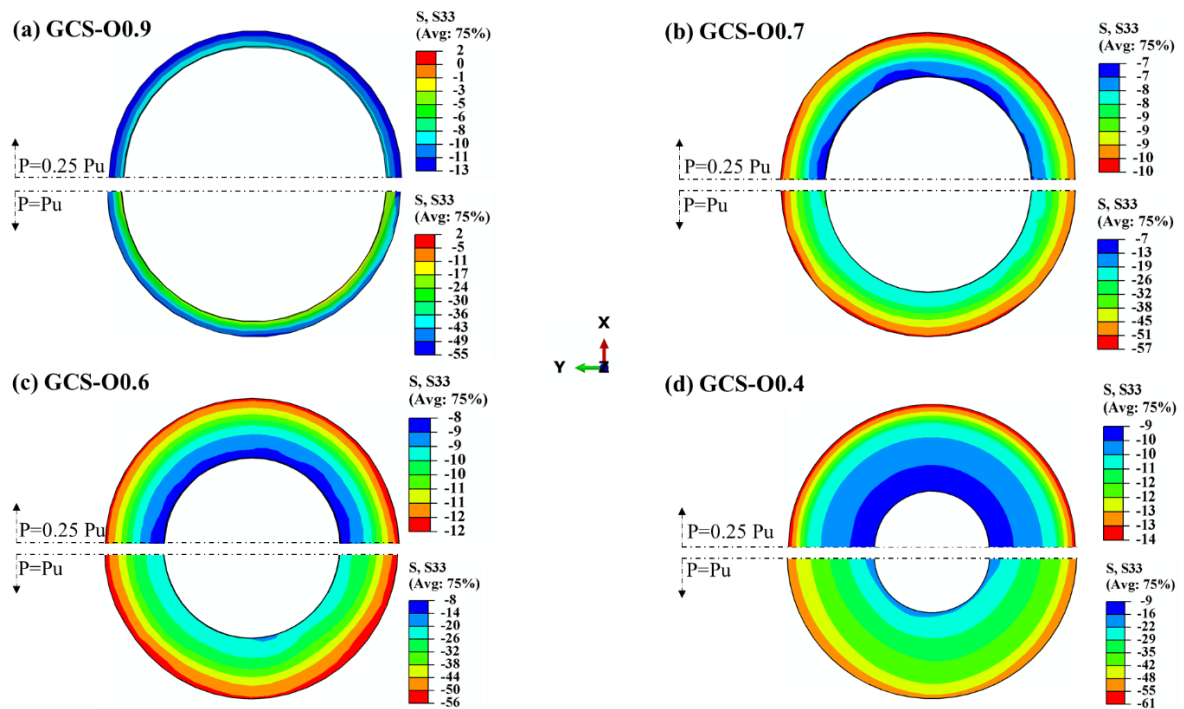
298 Figure 9: Effect of steel tube cross section on the axial compressive strength of FE models in group GCL for a)  
 299 constant external tube and b) constant inner tube

#### 300 4.2 Effect of grout thickness

301 For the GCS group with  $D/t=80$ , the axial stresses for increasing grout thickness are visualised  
 302 in Figure 10. The grout thicknesses at Figures 10(a) to 10(d) were 6.35 mm, 24.51 mm, 38.13 mm and  
 303 85.81 mm and the corresponding ultimate loads  $P_u$  were 436.99 kN, 871.11 kN, 1260.64 kN, 3099.45  
 304 kN respectively. In all cases, the bottom cross-section shows the stress distribution in  $N/mm^2$  when the  
 305 failure load ( $P_u$ ) was reached and the top cross section shows the stresses at  $P=0.25P_u$ , during the elastic  
 306 stage of the load-axial shortening curve. For the examined FE models, the stresses on the grout core  
 307 indicate a smooth transition along the thickness during the elastic stage. For example for the models  
 308 with intermediate thicknesses (see Figure 10(b) and (c)), the stresses appear to be in the range of 7 to  
 309 10  $N/mm^2$  and 8 to 12  $N/mm^2$  for  $0.25 P_u$ , respectively. Similar are the conclusions for the specimens  
 310 with higher and lower grout thickness.

311 On the contrary, once the ultimate load is reached the distribution of stresses from the inner to  
 312 the outer steel tube, is significantly higher for all models. For example as shown in Figure 10(d), the  
 313 concrete stresses closer to the inner tube are as low as 9  $N/mm^2$  and reach values as high as 61  $N/mm^2$   
 314 once closer to the external tube, demonstrating an increase of 52  $N/mm^2$  towards the outer tube. Similar

315 is the range for all four cases of Figure 10 with an axial stress range within 48 - 57 N/mm<sup>2</sup>. This is  
 316 owing to the larger confinement that is provided on the grout core from the external steel tube when  
 317 compared to the internal tube. This is also in agreement with findings presented in section 4.1.



318  
 319 Figure 10: Distribution of stresses on concrete core for varying hollow ratio and constant  $D/t=80$

320 Typical failure modes that were observed in the numerical models are shown in Figure 11. For  
 321 sections with large hollow ratio values – hence, small grout core thickness, the lateral restraint was less  
 322 pronounced, leading to local instabilities at locations where higher compressive steel stresses occurred,  
 323 as shown in Figure 11a. As it can be observed in Figure 11b and Figure 11c, for  $Dt60$  and  $Dt70$  the  
 324 compressive stresses led to a local instability in the external steel tube, resulting in a failure mode similar  
 325 to “elephant foot” buckling. For larger grout thicknesses (Figure 11d), material yielding was the  
 326 prominent failure mode. Finally, it is noted that the deformed shape of the model shown in Figure 11a  
 327 corresponds to high applied deformations, well beyond the ultimate load. It is believed that despite the  
 328 symmetry in terms of geometry, loading and boundary conditions, a non-symmetric deformed shape  
 329 can occur either as the result numerical instabilities/roundoff errors that start off as infinitesimal but  
 330 propagate and accumulate throughout the analysis thus becoming significant or due to the bifurcation  
 331 of the symmetric solution to non-symmetric ones. This secondary bifurcation has been observed  
 332 experimentally [48] and discussed analytically [49] for circular tubes in compression and it is believed  
 333 that it can occur for the type of structures studied herein, albeit, the presence of concrete infill makes  
 334 the switching from an axisymmetric model to a non-axisymmetric one more difficult.

335

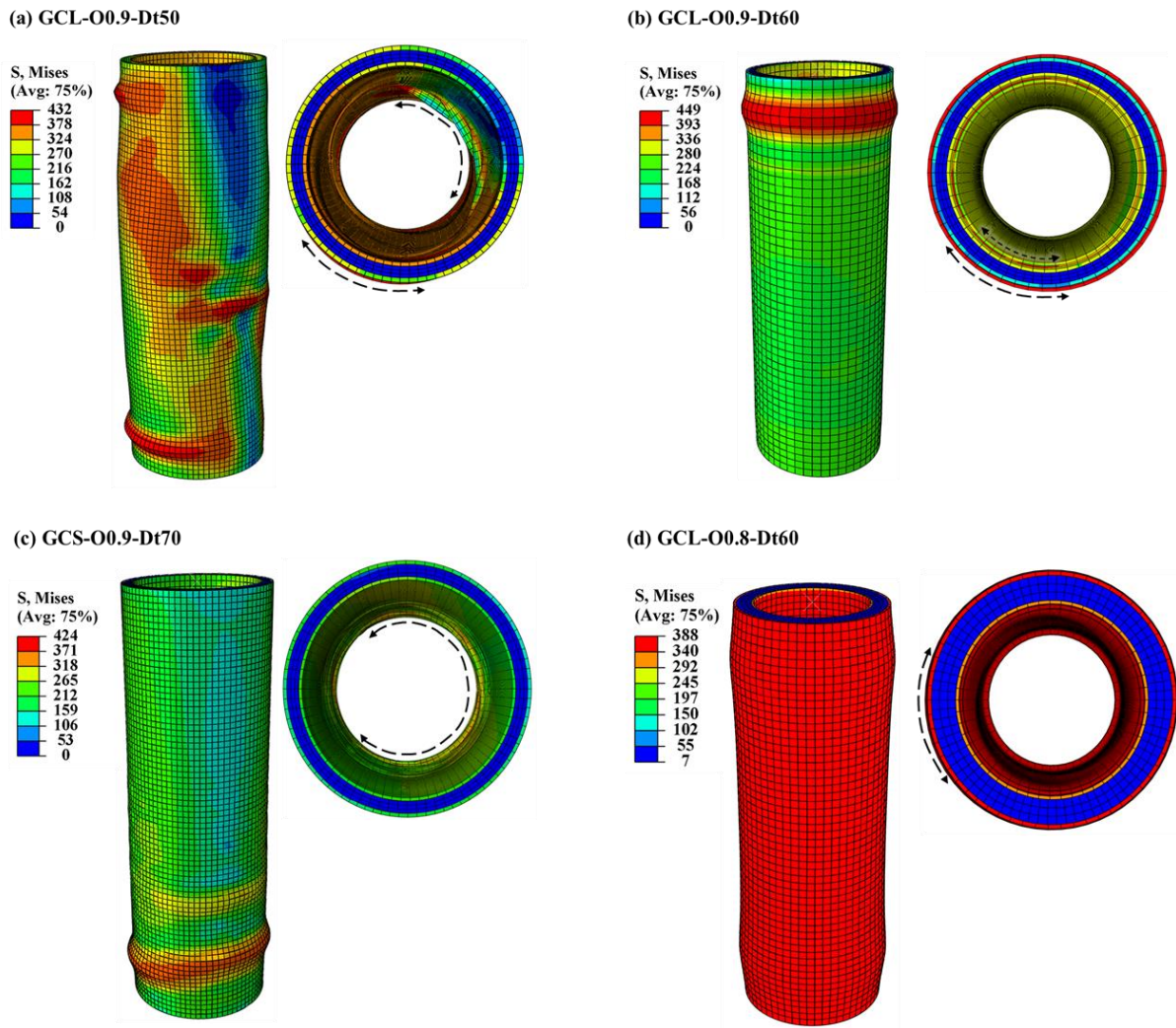


Figure 11: Typical failure modes from FE models for varying cross-sectional slenderness

## 5 Design Predictions

The data generated from the parametric study alongside experimental data collected from the literature, were employed to assess previously proposed design equations and code specifications and their applicability to GFDST stub-columns. For this purpose, the design equations provided in EC4 [36] and in the ACI code [37] for concrete filled members are modified to be applicable for double-skin tubular steel members and assessed herein. In addition, the analytical models proposed in [8] and [38] are also evaluated. The accuracy of the aforementioned four different design approaches to accurately predict the resistance of double skin cross-sections in compression at ultimate limit state has been assessed.

In sections 5.1-5.4, the design equations that were used, along with the modifications made are presented in detail. The presently generated numerical data along with literature collated data are summarised and compared to the design guidelines in section 5.5.

350 5.1 Eurocode 4 (EN 1994-1-1)

351 EN 1994-1-1 (EC4) [36] provides general rules for the design of composite steel-concrete  
 352 columns and composite structures in compression. Even though the plastic resistance of concrete-filled  
 353 tubes in compression is detailed in Section 6.7.3.2 [36], the design of filled double-skin steel members  
 354 is not currently covered by Eurocodes, thus a modification to existing methods was made. EC4 provides  
 355 a design equation for concrete-filled steel tubes with reinforcement by means of a resistance function.  
 356 The plastic resistance in compression  $N_{pl,Rd}$  is the summation of the resistance of the components  
 357 forming the cross-section under investigation. The latter has been modified for GFDSTs to include the  
 358 grout infill and the internal steel tube replaces the steel reinforcement as per equation (14). Similar  
 359 modifications to EC4 have been employed by Wang et al. [27], for double-skinned sections formed by  
 360 stainless and high strength steel tubes.

$$P_{EC4} = \eta_a A_{so} f_{sy0} + A_g f_c \left( 1 + \eta_c \frac{t_o f_{sy0}}{D_o f_c} \right) + A_{si} f_{syi} \quad (14)$$

361 where  $f_c$  is the compressive cylinder strength of the grout and,  $\eta_a$   $\eta_c$  and are given by equations (15) and  
 362 (16),

$$\eta_a = 0.25(3 + 2\bar{\lambda}) \leq 1.0 \quad (15)$$

$$\eta_c = 4.9 - 18.5\bar{\lambda} + 17\bar{\lambda}^2 \geq 0 \quad (16)$$

363 where  $\bar{\lambda}$  is the relative slenderness as described in equation (17):

$$\bar{\lambda} = \sqrt{\frac{N_{pl,Rk}}{N_{cr}}} \quad (17)$$

364 where  $N_{pl,Rk}$  is the characteristic value of the plastic resistance to compression given by equation (18)  
 365 and evaluated as a sum of forces of the constituent elements. For the grout core a unity coefficient has  
 366 been employed to take into consideration the confinement effects.

$$N_{pl,Rk} = A_{so} f_{sy0} + A_g f_c + A_{si} f_{syi} \quad (18)$$

367 The elastic critical buckling load ( $N_{cr}$ ), is calculated with the elastic effective stiffness ( $EI_{eff}$ ), according  
 368 to equation (19),

$$EI_{eff} = E_{so} I_{so} + E_{si} I_{si} + K_e E_g I_g \quad (19)$$

369 where  $K_e$  is a correction factor for the grout core equal to 0.6,  $E$  the Young's modulus and the second  
 370 moment of area ( $I$ ) for each of the components of the cross-section. According to EC 4, for circular  
 371 hollow steel sections if the local slenderness limit as defined in (20) is exceeded, local buckling ought  
 372 to be accounted for,

$$D/t \leq 90 \left( \frac{235}{f_{sy}} \right) \quad (20)$$

373 For this reason for the subsequent EC4 calculation, the cross section of the steel tubes was modified to  
 374 account for local buckling according to equation (21) proposed in [50] and has been recently employed  
 375 by Wang et al. [27], for CFDST stub-columns with external stainless steel tube.

$$A_{seo,i} = A_{so,i} \left( \frac{90}{D_{o,i}/t_{o,i}} \frac{235}{f_{syo,i}} \frac{E_{o,i}}{210000} \right)^{0.5} \quad (21)$$

376 where, the subscripts (o, i) refer to the external and internal steel tube.

## 377 5.2 American Concrete Institute (ACI)

378 ACI [37] which is the American code for the design of concrete structures provides design  
 379 formula for the evaluation of the ultimate strength of concrete-filled circular short columns.  
 380 Incorporating the contribution of the inner tube, the compressive cross-sectional strength ( $P_{ACI}$ ) of  
 381 concrete-filled tubes is modified to equation (22) as follows:

$$P_{ACI} = A_{so} f_{syo} + 0.85 A_g f_c + A_{si} f_{syi} \quad (22)$$

## 382 5.3 Han et al. [8]

383 Han et al. carried out a series of experiments on CFDST stub columns and proposed a new design  
 384 equation (23) for the ultimate strength of CFDST cross-sections, also considering the confinement  
 385 offered to the core from the external steel tube and the influence of the hollow ratio:

$$P_{Han} = A_{sco} f_{scy0} + A_{si} f_{syi} \quad (23)$$

386 The first term corresponds to the compressive capacity of the external steel tube alongside the  
 387 sandwiched grout and the second term to the compressive capacity of the internal steel tube. The cross-  
 388 sectional area  $A_{sco}$ , is given from equation (24)

$$A_{sco} = A_{so} + A_g \quad (24)$$

389 and  $f_{scy0}$  is given by equation (25),

$$f_{scy0} = k_1 C_1 \chi^2 f_{syo} + C_2 (1.14 + 1.02 \xi) f_c \quad (25)$$

390 where the coefficients  $C_1$ ,  $C_2$  and the confinement factor ( $\xi$ ) are calculated according to equations (26)  
 391 and (27):

$$C_1 = \frac{a}{1+a}, C_2 = \frac{1+a_n}{1+a} \quad (26)$$

$$\xi = a_n \frac{f_{scyo}}{f_c} \quad (27)$$

392 where  $a$  and  $a_n$  are the steel ratio and the nominal steel ratio as follows:

$$a = \frac{A_{so}}{A_g}, a_n = \frac{A_{so}}{A_{g,nom}} \quad (28)$$

393 where the nominal cross-section of the sandwiched grout ( $A_{g,nom}$ ) is:

$$A_{g,nom} = \frac{\pi(D_o - 2t_o)^2}{4} \quad (29)$$

#### 394 5.4 Yu et al. [38]

395 Yu et al. proposed a unified equation for the estimate of ultimate compressive strength of  
 396 concrete-filled tubes in compression. To include the internal steel tube, the modification suggested in  
 397 Hassanein and Kharoob [10] is used herein following Equation (30),

$$P_{Yu,mod} = (A_{so}f_{syo} + A_gf_c) \left( 1 + 0.5 \frac{\xi}{1 + \xi} \Omega \right) + A_{si}f_{syi} \quad (30)$$

398 where the solid ratio,  $\Omega$  is defined as per equation (31),  $A_k$  the hollow area as depicted in Figure 1 and  
 399 the rest as previously defined:

$$\Omega = \frac{A_g}{A_g + A_k} \quad (31)$$

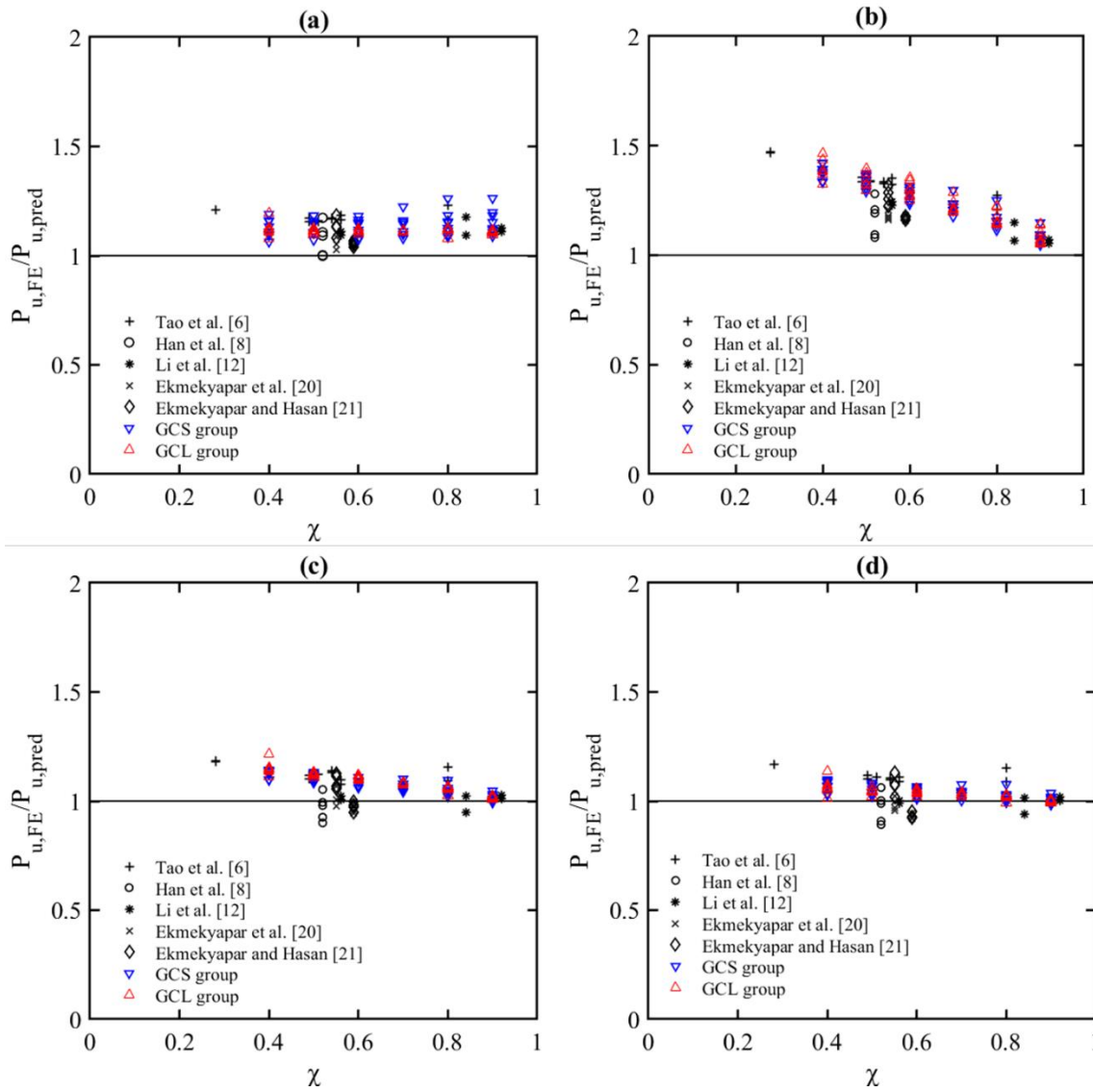
#### 400 5.5 Assessment of design predictions

401 In order to evaluate the suitability of design prediction methods, the bearing capacity of the FE  
 402 models is normalised against the analytically-obtained strength predictions ( $P_{EC4}$ ,  $P_{ACI}$ ,  $P_{Han}$  and  $P_{Yu,mod}$ )  
 403 and is shown in a tabulated format for the small (GCS) and large diameter (GCL) groups, in Table 3  
 404 and Table 4 respectively. Collated test data from the literature [6, 8, 12, 20, 21], are also employed for  
 405 assessment purposes and are shown in Table 5 in a similar format, by normalising test results against  
 406 design predictions. For both groups of the FE models and collated data it is found that the strength  
 407 predictions are on the safe side with varying levels of conservatism and scatter as shown in Figure 12,  
 408 where the ultimate sustained load is normalised with the predicted capacity from each design method  
 409 and presented against the examined hollow ratios. EC4 yielded safe predictions with similar trends for  
 410 both groups, with an average of 1.136 and 1.113 for GCS and GCL groups respectively. An increasing  
 411 conservatism with increasing hollow ratio values is observed to be consistent for small and large-  
 412 diameter models (Figure 12a). The conservatism for high slenderness is possibly attributed to the local  
 413 buckling limit suggested in [36], which is currently not explicitly defined for double skin filled tubular

414 members, but hollow steel members. In this case local buckling limit was taken equal to class 3 hollow  
415 sections, which does not account for the lateral restraint from the infill material.

416 The design predictions from ACI were found to be the most conservative amongst the design  
417 methods. Particularly for smaller hollow ratios (0.4-0.6) a high level of conservatism is shown, whereas  
418 this reduces for models with large hollow ratios (Figure 12b). In addition, for all the investigated models  
419 a high scatter was observed when this method was employed, which can be associated with the fact that  
420 ACI does not account for confinement effects. Similar findings were also reported for CFDST stub-  
421 columns with external stainless steel tubes in Wang et al. [27]. Predictions obtained from Han et al. [8]  
422 were also found on the safe side with a small scatter and an average of 1.076 for GCS and 1.088 for  
423 GCL models (Figure 12c). Strength predictions for models with hollow ratios of 0.8 and 0.9 are closer  
424 to unity and overall with less conservatism compared to EC4 and ACI. Yu et al. [38] model results in  
425 good predictions close to unity with reduced conservatism (Figure 12d) and a coefficient of variation  
426 of 0.029 (GCS group) and 0.025 (GCL group). Overall, it is shown that the modified Yu et al. strength  
427 predictions are of lower conservatism. Nevertheless, Han et al. and EC4 methods can also be used for  
428 design purposes of GFDST members as the vast majority of the models are on the safe side.





429

430

431

Figure 12: Comparison of FE obtained compressive strength to design strength predictions for small diameter (group GCS) and large diameter (group GCL) models with a) EC4, b) ACI, c) Han et al. [8], d) Yu et al. [38]

Table 3: Comparisons of small diameter FE model with design strength predictions

Group	FE model ID	D/t	D <sub>o</sub> (mm)	t <sub>o</sub> (mm)	D <sub>i</sub> (mm)	t <sub>i</sub> (mm)	L (mm)	$\chi$	$\frac{P_{u,EC4}}{P_{u,FE}}$	$\frac{P_{u,ACI}}{P_{u,FE}}$	$\frac{P_{u,Han}}{P_{u,FE}}$	$\frac{P_{u,Yu,mod}}{P_{u,FE}}$			
GCS1	I0.9-Dt50	50	140.0	2.80	120.9	2.41	420.0	0.9	1.125	1.080	1.031	1.015			
	I0.8-Dt50				107.5	2.15		0.8	1.126	1.156	1.060	1.031			
	I0.7-Dt50				94.0	1.88		0.7	1.110	1.206	1.067	1.027			
	I0.6-Dt50				80.6	1.61		0.6	1.118	1.273	1.092	1.043			
	I0.5-Dt50				67.2	1.34		0.5	1.103	1.306	1.093	1.037			
	I0.4-Dt50				53.7	1.07		0.4	1.094	1.337	1.096	1.034			
	O0.9-Dt50				131.9	2.63		114.0	2.28	395.8	0.9	1.089	1.046	0.998	0.983
	O0.8-Dt50				148.4	2.96		445.3	0.8	1.085	1.114	1.021	0.994		
	O0.7-Dt50				169.6	3.39		508.9	0.7	1.079	1.176	1.042	1.002		
	O0.6-Dt50				197.9	3.95		593.7	0.6	1.073	1.233	1.061	1.010		
O0.5-Dt50	237.5	4.75	712.5	0.5	1.071	1.290	1.084	1.022							
O0.4-Dt50	296.8	5.93	890.6	0.4	1.063	1.333	1.099	1.028							
GCS2	I0.9-Dt60	60	140.0	2.33	121.8	2.03	420.0	0.9	1.118	1.074	1.022	1.008			
	I0.8-Dt60				108.2	1.80		0.8	1.096	1.132	1.034	1.008			
	I0.7-Dt60				94.7	1.57		0.7	1.098	1.204	1.061	1.026			
	I0.6-Dt60				81.2	1.35		0.6	1.106	1.273	1.089	1.045			
	I0.5-Dt60				67.6	1.12		0.5	1.106	1.323	1.105	1.055			
	I0.4-Dt60				54.1	0.90		0.4	1.110	1.370	1.122	1.066			
	O0.9-Dt60				131.0	2.18		114	1.90	393.1	0.9	1.106	1.062	1.010	0.997
	O0.8-Dt60				147.4	2.45		442.2	0.8	1.113	1.150	1.050	1.024		
	O0.7-Dt60				168.4	2.80		505.4	0.7	1.111	1.221	1.077	1.040		
	O0.6-Dt60				196.5	3.27		589.6	0.6	1.078	1.248	1.071	1.025		
O0.5-Dt60	235.8	3.93	707.5	0.5	1.108	1.342	1.126	1.068							
O0.4-Dt60	294.8	4.91	884.4	0.4	1.096	1.379	1.137	1.070							
GCS3	I0.9-Dt70	70	140.0	2.00	122.4	1.74	420.0	0.9	1.183	1.094	1.031	1.019			
	I0.8-Dt70				108.8	1.55		0.8	1.156	1.157	1.046	1.024			
	I0.7-Dt70				95.2	1.36		0.7	1.145	1.220	1.067	1.036			
	I0.6-Dt70				81.6	1.16		0.6	1.146	1.283	1.090	1.053			
	I0.5-Dt70				68.0	0.97		0.5	1.151	1.341	1.114	1.071			
	I0.4-Dt70				54.4	0.77		0.4	1.157	1.390	1.134	1.086			
	O0.9-Dt70				130.3	1.86		114	1.62	391.1	0.9	1.153	1.066	1.005	0.993
	O0.8-Dt70				146.6	2.09		440.0	0.8	1.151	1.152	1.042	1.020		
	O0.7-Dt70				167.6	2.39		502.9	0.7	1.153	1.232	1.079	1.046		
	O0.6-Dt70				195.5	2.79		586.7	0.6	1.152	1.297	1.109	1.067		
O0.5-Dt70	234.7	3.35	704.1	0.5	1.148	1.358	1.133	1.083							
O0.4-Dt70	293.3	4.19	880.1	0.4	1.133	1.393	1.143	1.085							
GCS4	I0.9-Dt80	80	140.0	1.75	122.8	1.53	420.0	0.9	1.263	1.149	1.047	1.037			
	I0.8-Dt80				109.2	1.36		0.8	1.261	1.250	1.096	1.077			
	I0.7-Dt80				95.5	1.19		0.7	1.224	1.297	1.102	1.076			
	I0.6-Dt80				81.9	1.02		0.6	1.181	1.317	1.092	1.061			
	I0.5-Dt80				68.2	0.85		0.5	1.183	1.373	1.116	1.080			
	I0.4-Dt80				54.6	0.68		0.4	1.190	1.422	1.139	1.099			
	O0.9-Dt80				129.9	1.62		114.0	1.42	389.7	0.9	1.198	1.090	0.993	0.983
	O0.8-Dt80				146.1	1.82		438.4	0.8	1.184	1.174	1.030	1.011		
	O0.7-Dt80				167.0	2.08		501.0	0.7	1.161	1.236	1.050	1.025		
	O0.6-Dt80				194.8	2.43		584.6	0.6	1.164	1.309	1.088	1.053		
O0.5-Dt80	233.8	2.92	701.5	0.5	1.159	1.364	1.114	1.071							
O0.4-Dt80	292.3	3.65	876.9	0.4	1.161	1.420	1.143	1.093							
<b>Average</b>									<b>1.136</b>	<b>1.244</b>	<b>1.076</b>	<b>1.040</b>			
<b>COV</b>									<b>0.040</b>	<b>0.085</b>	<b>0.038</b>	<b>0.029</b>			

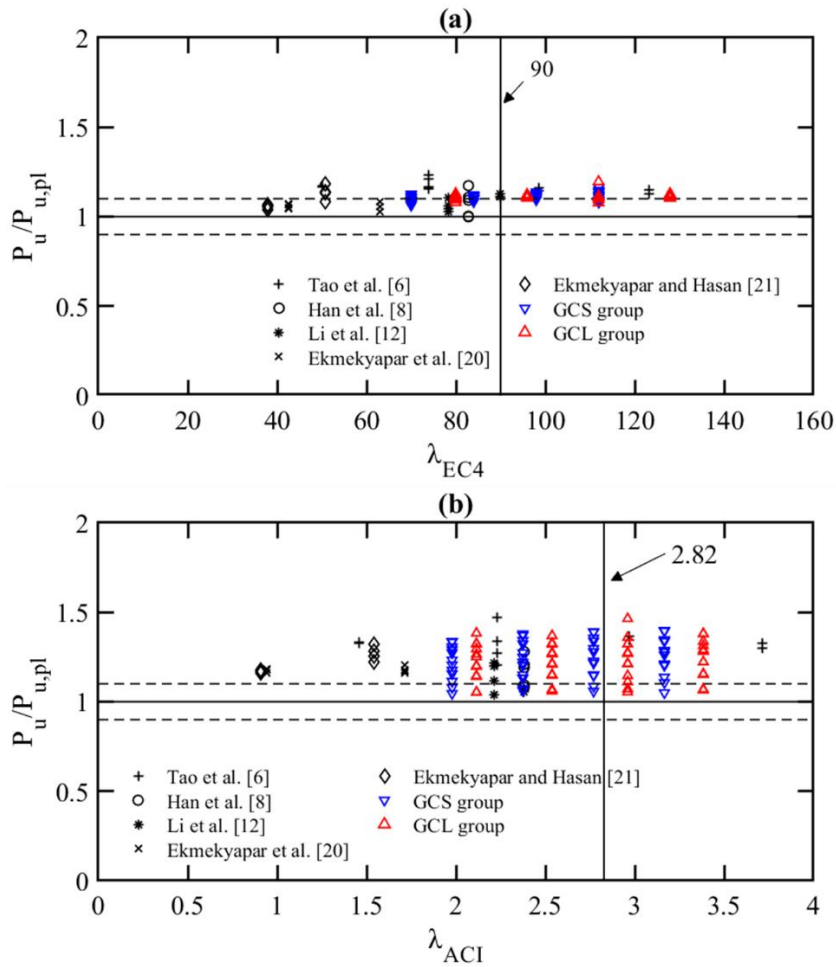
Table 4: Comparisons of large diameter FE model with design strength predictions

Group	FE model ID	D/t	D <sub>o</sub> (mm)	t <sub>o</sub> (mm)	D <sub>i</sub> (mm)	t <sub>i</sub> (mm)	L (mm)	$\chi$	$\frac{P_{u,EC4}}{P_{u,FE}}$	$\frac{P_{u,ACI}}{P_{u,FE}}$	$\frac{P_{u,Han}}{P_{u,FE}}$	$\frac{P_{u,Yu,mod}}{P_{u,FE}}$						
GCL1	I0.9-Dt50	50	450.0	9.00	388.8	7.77	1350.0	0.9	1.101	1.052	1.010	0.990						
	I0.8-Dt50								1.121	1.145	1.061	1.021						
	I0.7-Dt50								1.111	1.201	1.077	1.021						
	I0.6-Dt50								1.113	1.265	1.102	1.032						
	I0.5-Dt50								1.116	1.322	1.124	1.042						
	I0.4-Dt50								1.128	1.383	1.153	1.060						
	O0.9-Dt50								462.9	9.25	400.0	8.00	1388.9	0.9	1.103	1.054	1.012	0.992
	O0.8-Dt50								520.8	10.41			1562.5	0.8	1.118	1.141	1.057	1.017
	O0.7-Dt50								595.2	11.90			1785.7	0.7	1.107	1.197	1.075	1.018
	O0.6-Dt50								694.4	13.88			2083.3	0.6	1.100	1.250	1.093	1.020
	O0.5-Dt50								833.3	16.66			2500.0	0.5	1.093	1.295	1.107	1.020
O0.4-Dt50	1041.7	20.83			3125.0	0.4	1.079	1.325	1.111	1.012								
GCL2	I0.9-Dt60	60	450.0	7.50	391.5	6.52	1350.0	0.9	1.136	1.059	1.015	0.996						
	I0.8-Dt60								1.145	1.147	1.060	1.022						
	I0.7-Dt60								1.135	1.209	1.081	1.028						
	I0.6-Dt60								1.130	1.267	1.101	1.036						
	I0.5-Dt60								1.129	1.321	1.122	1.046						
	I0.4-Dt60								1.132	1.369	1.141	1.056						
	O0.9-Dt60								459.77	7.66	400.0	6.66	1379.3	0.9	1.146	1.068	1.024	1.004
	O0.8-Dt60								517.24	8.62			1551.7	0.8	1.150	1.152	1.065	1.026
	O0.7-Dt60								591.13	9.85			1773.4	0.7	1.140	1.214	1.087	1.032
	O0.6-Dt60								689.65	11.49			2068.9	0.6	1.135	1.273	1.110	1.040
	O0.5-Dt60								827.58	13.79			2482.8	0.5	1.134	1.326	1.132	1.048
O0.4-Dt60	1034.48	17.24			3103.4	0.4	1.129	1.368	1.147	1.051								
GCL3	I0.9-Dt70	70	450.0	6.42	393.4	5.62	1350.0	0.9	1.200	1.085	1.008	0.990						
	I0.8-Dt70								1.198	1.175	1.054	1.019						
	I0.7-Dt70								1.182	1.240	1.079	1.030						
	I0.6-Dt70								1.170	1.297	1.100	1.040						
	I0.5-Dt70								1.166	1.350	1.121	1.051						
	I0.4-Dt70								1.174	1.464	1.217	1.135						
	O0.9-Dt70								457.5	6.53	400.0	5.71	1372.5	0.9	1.220	1.103	1.025	1.006
	O0.8-Dt70								514.7	7.35			1544.1	0.8	1.163	1.140	1.024	0.989
	O0.7-Dt70								588.2	8.40			1764.7	0.7	1.186	1.243	1.084	1.033
	O0.6-Dt70								686.2	9.80			2058.8	0.6	1.176	1.303	1.108	1.044
	O0.5-Dt70								823.5	11.76			2470.5	0.5	1.166	1.350	1.126	1.049
O0.4-Dt70	1029.4	14.70			3088.2	0.4	1.154	1.385	1.138	1.050								
GCL4	I0.9-Dt80	80	450.0	5.62	394.8	4.93	1350.0	0.9	1.273	1.136	1.017	0.999						
	I0.8-Dt80								1.250	1.220	1.056	1.024						
	I0.7-Dt80								1.229	1.287	1.085	1.040						
	I0.6-Dt80								1.211	1.342	1.106	1.051						
	I0.5-Dt80								1.204	1.395	1.128	1.065						
	I0.4-Dt80								1.199	1.437	1.145	1.075						
	O0.9-Dt80								455.8	5.69	400.0	5.00	1367.5	0.9	1.279	1.141	1.021	1.004
	O0.8-Dt80								512.8	1.82			1538.4	0.8	1.256	1.225	1.062	1.029
	O0.7-Dt80								586.0	2.08			1758.2	0.7	1.231	1.289	1.088	1.041
	O0.6-Dt80								683.7	2.43			2051.2	0.6	1.222	1.353	1.118	1.058
	O0.5-Dt80								820.5	10.25			2461.5	0.5	1.185	1.373	1.114	1.045
O0.4-Dt80	1025.6	12.82			3076.9	0.4	1.196	1.437	1.151	1.070								
<b>Average</b>									<b>1.113</b>	<b>1.231</b>	<b>1.088</b>	<b>1.033</b>						
<b>COV</b>									<b>0.014</b>	<b>0.088</b>	<b>0.042</b>	<b>0.025</b>						

Table 5: Comparisons of collated test data with design strength predictions

Source	Test ID	$\frac{P_{u,EC4}}{P_{u,Test}}$	$\frac{P_{u,ACI}}{P_{u,Test}}$	$\frac{P_{u,Han}}{P_{u,Test}}$	$\frac{P_{u,Yu,mod}}{P_{u,Test}}$
[6]	cc2a, cc2b, cc3a, cc3b, cc4a, cc4b, cc5a, cc5b, cc6a, cc6b, cc7a, cc7b	1.179	1.344	1.127	1.118
[8]	DC-1, DC-2, DCc-0, DCc-1, DCc-2	1.074	1.171	0.970	0.971
[12]	GC1-1, GC1-2, GC2-1, GC2-2, GCL-1, GCL-2	1.118	1.135	1.006	0.995
[20]	0-1-1-1, 0-1-1-2, 0-2-1-1, 0-2-1-2, 0-2-1-2, 0-1-2-1, 0-1-2-2, 0-2-2-1, 0-2-2-2	1.053	1.175	0.991	0.959
[21]	1-1-2, 2-1-2, 1-1-1, 2-1-1, 1-2-2, 2-2-2, 1-2-1, 2-2-1	1.095	1.221	1.033	1.007
<b>Average</b>		<b>1.113</b>	<b>1.230</b>	<b>1.041</b>	<b>1.025</b>
<b>COV</b>		<b>0.055</b>	<b>0.082</b>	<b>0.071</b>	<b>0.078</b>

436 In Figure 13, the ultimate capacity obtained from the collated test data or the presented FE models is  
 437 normalised against the plastic resistance design predictions from EC4 and ACI. In this case buckling of  
 438 the slender cross-sections is not considered, thus allowing to examine the applicability of the class 3  
 439 limit for GFDST stub-columns. The current limits for local buckling are also plotted for each design  
 440 method.



441

442 Figure 13 : Comparison of collated experimental data and FE models against strength predictions from a) EC4  
 443 and b) ACI

444 In Figure 13a, it is shown that strength predictions are on the safe side for GCS, GCL groups and also  
445 for the experimental data, hence it is suggested that further investigations are required to define a more  
446 appropriate slenderness limit for GFDST stub-columns, considering the lateral restraint provided by the  
447 infill material. This could potentially result in strength predictions with less conservatism. The ACI  
448 model, despite the ease of use resulted in very large scatter and conservatism for all the investigated  
449 data (Figure 13b). Considering local buckling improved the results as shown in Figure 12b, however  
450 further fine tuning of the model is required in order to consider confinement effects for varying cross-  
451 sections and strain hardening of steel tubes, to allow for less conservative results.

## 452 **6 Conclusions**

453 A comprehensive numerical investigation on the behaviour of tubular GFDST stub-columns was  
454 presented in this paper. The numerical models have been validated against experimental data from the  
455 literature, replicating the experimentally observed the load-displacement performance, the failure  
456 modes and the load capacity. A detailed description of the numerical considerations and assumptions  
457 was given and a parametric study, aiming to generate additional structural performance data and to  
458 evaluate the influence of key parameters has been carried out. The following conclusions were drawn:

- 459 - It was shown that the compressive capacity of GFDST stub-columns increases as the hollow  
460 ratio decreases. In most cases the GFDST stub-columns failed in a ductile manner once the  
461 peak load was reached.
- 462 - An investigation on the distribution of stresses laterally across the cross section of the  
463 examined models, showed that higher stresses occur close to the external steel tube for  
464 GFDSTs at ultimate capacity. This suggests that the confinement effect offered by the  
465 internal steel tube may be less pronounced for double skin sections.
- 466 - The modified design method of EC4 showed good strength predictions for both groups and  
467 is suggested that it may be employed for the design of GFDST stub-columns, however further  
468 studies are required to define an appropriate slenderness limit. On the contrary, ACI yielded  
469 the higher levels of conservatism, especially for hollow ratios between 0.4 and 0.6.
- 470 - Han et al. and the modified Yu et al. models produced good strength predictions with lower  
471 conservatism. Overall, Yu et al. results were superior to other methods with the smallest  
472 coefficient of variation for all groups. It should be noted that both models were specifically  
473 developed for double skin filled stub-columns.

474

475 **References**

- 476 [1] Espinos A, Romero ML, Serra E, Hospitaler A. Experimental investigation on the fire behaviour of  
477 rectangular and elliptical slender concrete-filled tubular columns. *Thin-Walled Struct* 2015;93:137–48.  
478 <https://doi.org/10.1016/j.tws.2015.03.018>
- 479 [2] Portolés JM, Romero ML, Bonet JL, Filippou FC. Experimental study of high strength concrete-  
480 filled circular tubular columns under eccentric loading. *J Constr Steel Res* 2011;67:623–33.  
481 <https://doi.org/10.1016/j.jcsr.2010.11.017>
- 482 [3] Han LH, Li W, Bjorhovde R. Developments and advanced applications of concrete-filled steel  
483 tubular (CFST) structures: Members. *J Constr Steel Res* 2014;100:211–28.  
484 <https://doi.org/10.1016/j.jcsr.2014.04.016>
- 485 [4] Vernardos S, Gantes C. Experimental behavior of concrete-filled double-skin steel tubular (CFDST)  
486 stub members under axial compression: A comparative review. *Structures* 2019;22:383–404.  
487 <https://doi.org/10.1016/j.istruc.2019.06.025>
- 488 [5] Giakoumelis G, Lam D. Axial capacity of circular concrete-filled tube columns. *J Constr Steel Res*  
489 2004;60:1049–68. <https://doi.org/10.1016/j.jcsr.2003.10.001>
- 490 [6] Tao Z, Han LH, Zhao XL. Behaviour of concrete-filled double skin (CHS inner and CHS outer)  
491 steel tubular stub columns and beam-columns. *J Constr Steel Res* 2004;60:1129–58.  
492 <https://doi.org/10.1016/j.jcsr.2003.11.008>
- 493 [7] Zhao XL, Tong LW, Wang XY. CFDST stub columns subjected to large deformation axial loading.  
494 *Eng Struct* 2010;32:692–703. <https://doi.org/10.1016/j.engstruct.2009.11.015>
- 495 [8] Han LH, Li YJ, Liao FY. Concrete-filled double skin steel tubular (CFDST) columns subjected to  
496 long-term sustained loading. *Thin-Walled Struct* 2011;49:1534–43.  
497 <https://doi.org/10.1016/j.tws.2011.08.001>
- 498 [9] Hu HT, Su FC. Nonlinear analysis of short concrete-filled double skin tube columns subjected to  
499 axial compressive forces. *Mar Struct* 2011;24:319–37. <https://doi.org/10.1016/j.marstruct.2011.05.001>
- 500 [10] Hassanein MF, Kharoob OF. Compressive strength of circular concrete-filled double skin tubular  
501 short columns. *Thin-Walled Struct* 2014;77:165–73. <https://doi.org/10.1016/j.tws.2013.10.004>
- 502 [11] Tziavos NI, Hemida H, Dirar S, Papaelias M, Metje N, Baniotopoulos C. Structural health  
503 monitoring of grouted connections for offshore wind turbines by means of acoustic emission: An  
504 experimental study. *Renew Energy* 2020;147:130–40. <https://doi.org/10.1016/j.renene.2019.08.114>
- 505 [12] Li W, Wang D, Han LH. Behaviour of grout-filled double skin steel tubes under compression and  
506 bending: Experiments. *Thin-Walled Struct* 2017;116:307–19.  
507 <https://doi.org/10.1016/j.tws.2017.02.029>

- 508 [13] Wang FC, Han LH. Analytical behavior of carbon steel-concrete-stainless steel double-skin tube  
509 (DST) used in submarine pipeline structure. *Mar Struct* 2019;63:99–116.  
510 <https://doi.org/10.1016/j.marstruc.2018.09.001>
- 511 [14] Patel VI, Liang QQ, Hadi MNS. Numerical analysis of circular double-skin concrete-filled  
512 stainless steel tubular short columns under axial loading. *Structures* 2020;24:754–65.  
513 <https://doi.org/10.1016/j.istruc.2020.02.001>
- 514 [15] Liang QQ, Fragomeni S. Nonlinear analysis of circular concrete-filled steel tubular short columns  
515 under axial loading. *J Constr Steel Res* 2009;65:2186–96. <https://doi.org/10.1016/j.jcsr.2009.06.015>
- 516 [16] Han LH, Tao Z, Huang H, Zhao XL. Concrete-filled double skin (SHS outer and CHS inner) steel  
517 tubular beam-columns. *Thin-Walled Struct* 2004;42:1329–55.  
518 <https://doi.org/10.1016/j.tws.2004.03.017>
- 519 [17] Uenaka K, Kitoh H, Sonoda K. Concrete filled double skin circular stub columns under  
520 compression. *Thin-Walled Struct* 2010;48:19–24. <https://doi.org/10.1016/j.tws.2009.08.001>
- 521 [18] Wei S, Mau ST, Vipulanandan C, Mantrala SK. Performance of new sandwich tube under axial  
522 loading: Experiment. *J Struct Eng* 1995;121:1806–14. [https://doi.org/10.1061/\(ASCE\)0733-  
523 9445\(1995\)121:12\(1806\)](https://doi.org/10.1061/(ASCE)0733-9445(1995)121:12(1806))
- 524 [19] Essopjee Y, Dundu M. Performance of concrete-filled double-skin circular tubes in compression.  
525 *Compos Struct* 2015;133:1276–83. <https://doi.org/10.1016/j.compstruct.2015.08.033>
- 526 [20] Ekmekyapar T, Alwan OH, Hasan HG, Shehab BA, AL-Eliwi BJM. Comparison of classical,  
527 double skin and double section CFST stub columns: Experiments and design formulations. *J Constr  
528 Steel Res* 2019;155:192–204. <https://doi.org/10.1016/j.jcsr.2018.12.025>
- 529 [21] Ekmekyapar T, Ghanim Hasan H. The influence of the inner steel tube on the compression  
530 behaviour of the concrete filled double skin steel tube (CFDST) columns. *Mar Struct* 2019;66:197–212.  
531 <https://doi.org/10.1016/j.marstruc.2019.04.006>
- 532 [22] Zhao XL, Grzebieta R. Strength and ductility of concrete filled double skin (SHS inner and SHS  
533 outer) tubes. *Thin-Walled Struct* 2002;40:199–213. [https://doi.org/10.1016/S0263-8231\(01\)00060-X](https://doi.org/10.1016/S0263-8231(01)00060-X)
- 534 [23] Tao Z, Han LH. Behaviour of concrete-filled double skin rectangular steel tubular beam-columns.  
535 *J Constr Steel Res* 2006;62:631–46. <https://doi.org/10.1016/j.jcsr.2005.11.008>
- 536 [24] Han LH, Huang H, Tao Z, Zhao XL. Concrete-filled double skin steel tubular (CFDST) beam-  
537 columns subjected to cyclic bending. *Eng Struct* 2006;28:1698–714.  
538 <https://doi.org/10.1016/j.engstruct.2006.03.004>

- 539 [25] Aghdamy S, Thambiratnam DP, Dhanasekar M, Saiedi S. Effects of load-related parameters on  
540 the response of concrete-filled double-skin steel tube columns subjected to lateral impact. *J Constr Steel*  
541 *Res* 2017;138:642–62. <https://doi.org/10.1016/j.jcsr.2017.08.015>
- 542 [26] Huang H, Han LH, Zhao XL. Investigation on concrete filled double skin steel tubes (CFDSTs)  
543 under pure torsion. *J Constr Steel Res* 2013;90:221–34. <https://doi.org/10.1016/j.jcsr.2013.07.035>
- 544 [27] Wang F, Young B, Gardner L. Compressive testing and numerical modelling of concrete-filled  
545 double skin CHS with austenitic stainless steel outer tubes. *Thin-Walled Struct* 2019;141:345–59.  
546 <https://doi.org/10.1016/j.tws.2019.04.003>
- 547 [28] Wang F, Young B, Gardner L. CFDST sections with square stainless steel outer tubes under axial  
548 compression: Experimental investigation, numerical modelling and design. *Eng Struct*  
549 2020;207:110189. <https://doi.org/10.1016/j.engstruct.2020.110189>
- 550 [29] Wang F, Young B, Gardner L. Experimental Study of Square and Rectangular CFDST Sections  
551 with Stainless Steel Outer Tubes under Axial Compression. *J Struct Eng (United States)* 2019;145.  
552 [https://doi.org/10.1061/\(ASCE\)ST.1943-541X.0002408](https://doi.org/10.1061/(ASCE)ST.1943-541X.0002408)
- 553 [30] Zhou F, Young B. Concrete-filled double-skin aluminum circular hollow section stub columns.  
554 *Thin-Walled Struct* 2018;133:141–52. <https://doi.org/10.1016/j.tws.2018.09.037>
- 555 [31] Elchalakani M, Hassanein MF, Karrech A, Fawzia S, Yang B, Patel VI. Experimental tests and  
556 design of rubberised concrete-filled double skin circular tubular short columns. *Structures*  
557 2018;15:196–210. <https://doi.org/10.1016/j.istruc.2018.07.004>
- 558 [32] Pagoulatou M, Sheehan T, Dai XH, Lam D. Finite element analysis on the capacity of circular  
559 concrete-filled double-skin steel tubular (CFDST) stub columns. *Eng Struct* 2014;72:102–12.  
560 <https://doi.org/10.1016/j.engstruct.2014.04.039>
- 561 [33] Hassanein MF, Elchalakani M, Karrech A, Patel VI, Yang B. Behaviour of Concrete-filled Double-  
562 skin Short Columns Under Compression Through Finite Element Modelling: SHS Outer and SHS Inner  
563 Tubes. *Structures* 2018;14:358–75. <https://doi.org/10.1016/j.istruc.2018.04.006>
- 564 [34] Ding F xing, Wang W jun, Lu D ren, Liu X mei. Study on the behavior of concrete-filled square  
565 double-skin steel tubular stub columns under axial loading. *Structures* 2020;23:665–76.  
566 <https://doi.org/10.1016/j.istruc.2019.12.008>
- 567 [35] Duarte APC, Silva BA, Silvestre N, de Brito J, Júlio E, Castro JM. Finite element modelling of  
568 short steel tubes filled with rubberized concrete. *Compos Struct* 2016;150:28–40.  
569 <https://doi.org/10.1016/J.COMPSTRUCT.2016.04.048>
- 570 [36] EN 1994-1-1, Eurocode 4, Design of Composite Steel and Concrete Structures, Part 1.1: General  
571 Rules and Rules for Buildings, European Committee for Standardization (CEN), Brussels, 2004.



572 [37] ACI 318, Building Code Requirements for Structural Concrete and Commentary, Farmington  
573 Hills, Michigan, USA, 2014.

574 [38] Yu M, Zha X, Ye J, Li Y. A unified formulation for circle and polygon concrete-filled steel tube  
575 columns under axial compression. Eng Struct 2013;49:1–10.  
576 <https://doi.org/10.1016/j.engstruct.2012.10.018>

577 [39] ABAQUS, ABAQUS/standard User's Manual. Version 2019, Dassault Systemes Simulia Corp.,  
578 USA, 2019.

579 [40] Wang J, Afshan S, Gkantou M, Theofanous M, Baniotopoulos C, Gardner L. Flexural behaviour  
580 of hot-finished high strength steel square and rectangular hollow sections. J Constr Steel Res  
581 2016;121:97–109. <https://doi.org/10.1016/j.jcsr.2016.01.017>

582 [41] Tziavos NI, Hemida H, Metje N, Baniotopoulos C. Non-linear finite element analysis of grouted  
583 connections for offshore monopile wind turbines. Ocean Eng 2019;171:633–45.  
584 <https://doi.org/10.1016/j.oceaneng.2018.11.005>

585 [42] Mander JB, Priestley MJ, Park R, Theoretical stress-strain model for confined concrete. J Struct  
586 Eng 1988; 114 (8):1804-1826. [https://doi:10.1061/\(ASCE\)0733-9445\(1988\)114:8\(1804\)](https://doi:10.1061/(ASCE)0733-9445(1988)114:8(1804))

587 [43] Richart FE, Brandtzaeg A, Brown RL, A study of the failure of concrete under combined  
588 compressive stresses. University of Illinois at Urbana Champaign, (1973).

589 [44] Hu HT, Huang CS, Wu MH, Wu YM. Nonlinear analysis of axially loaded concrete-filled tube  
590 columns with confinement effect. J Struct Eng 2003;129:1322–9. [https://doi.org/10.1061/\(ASCE\)0733-  
591 9445\(2003\)129:10\(1322\)](https://doi.org/10.1061/(ASCE)0733-9445(2003)129:10(1322))

592 [45] Tao Z, Wang Z Bin, Yu Q. Finite element modelling of concrete-filled steel stub columns under  
593 axial compression. J Constr Steel Res 2013;89:121–31. <https://doi.org/10.1016/j.jcsr.2013.07.001>

594 [46] CEB-FIP CE. Model code 2010. Comite Euro-International du beton, 2010.

595 [47] Thai HT, Uy B, Khan M, Tao Z, Mashiri F. Numerical modelling of concrete-filled steel box  
596 columns incorporating high strength materials. J Constr Steel Res 2014;102:256–65.  
597 <https://doi.org/10.1016/j.jcsr.2014.07.014>

598 [48] Bardi FC, Kyriakides S. Plastic buckling of circular tubes under axial compression-part I:  
599 Experiments. Int J Mech Sci 2006;48:830–41. <https://doi.org/10.1016/j.ijmecsci.2006.03.005>

600 [49] Bardi FC, Kyriakides S, Yun HD. Plastic buckling of circular tubes under axial compression-part  
601 II: Analysis. Int J Mech Sci 2006;48:842–54. <https://doi.org/10.1016/j.ijmecsci.2006.03.002>

602 [50] Chan TM, Gardner L. Compressive resistance of hot-rolled elliptical hollow sections. Eng Struct  
603 2008;30:522–32. <https://doi.org/10.1016/j.engstruct.2007.04.019>